Research in Astronomy and Astrophysics, 23:095010 (9pp), 2023 September https://doi.org/10.1088/1674-4527/ace091

A Quasi-periodic Oscillation of ∼4.6 yr in the Radio Light Curves of Blazar PKS 0607-157

Xiao-Pan Li, Hai-Yan Yang, Yan Cai, Xie-Fei Song, Hai-Tao Yang, and Yu-Qiong Shan
College of Physics and Information Engineering, Zhaotong University, Zhaotong 657000, China; lxpzrc@163.com
Received 2023 January 3; revised 2023 June 9; accepted 2023 June 20; published 2023 July 31

Abstract

We present periodicity search analyses on long-term radio light curves at 4.8, 8, and 14.5 GHz of blazar PKS 0607–157 observed by the University of Michigan Radio Astronomical Observatory telescope. The highly variable radio emissions are approximately distributed as a log-normal probability distribution function. The Power Spectral Density for the radio light curves can be well characterized by a power-law model. Using the Weighted Wavelet Z-transform and Lomb-Scargle periodogram methods, significant Quasi-periodic Oscillation (QPO) of ∼4.6 yr in the radio light curve has been observed above the 3σ confidence level, which presents an interesting case among blazar QPO phenomena. We explore three plausible physical models to explain the observed QPOs: a supermassive binary black hole system, Lense-Thirring precession of the disk, and helical motion of plasma blobs within the jet.

Key words: galaxies: active – (galaxies:) BL Lacertae objects: general – (galaxies:) BL Lacertae objects: individual (PKS 0607-157)

1. Introduction

Active galactic nuclei (AGNs) are among the most energetic extragalactic sources in the universe with bolometric luminosity of 10^{41}–10^{48} erg s^{-1}, and are widely believed to be powered by the accretion process of the supermassive black holes (SMBHs) ranging between 10^6–$10^{10} M_\odot$ (e.g., Urry & Padovani 1995). Under the unified AGN paradigm, blazars belong to the most active subclass of AGNs with their relativistic jets nearly pointed to the observers. The continuum non-thermal emissions of blazars at entire wavelengths dominate the spectral energy distribution, and have been detected with timescales from few minutes to years. In general, their temporal behavior is usually considered to be driven by stochastic processes (e.g., Sobolewska et al. 2014; Vaughan et al. 2016; Kushwaha et al. 2017; Goyal et al. 2018; Tavani et al. 2018). Searching and explanation for the periodic signal in AGN light curves, however, have aroused significant attention since it can impose restrictions on the physical mechanisms causing blazar variability and optimize the scheduling of multi-wavelength studies.

It is becoming more and more noticeable that blazar light curves associated with their variability seem to exhibit an intriguing phenomenon known as quasi-periodic oscillation (QPO), which has been detected at all accessible timescales. Over the last few decades, a number of QPOs have been claimed for individual source in all detectable wave bands (e.g., Ackermann et al. 2015; Bhatta et al. 2016; Caproni et al. 2017; Zhang et al. 2017; Ren et al. 2021; Yang et al. 2021; Roy et al. 2022, and references therein), and a sample of AGNs mainly at γ-ray frequencies (e.g., Sandrinelli et al. 2016, 2018; Bhatta & Dhital 2020; Bhatta 2021; Peñil et al. 2020). However, on the other hand, several works expressed some caution about the QPO claims. For instance, Nilsson et al. (2018) analyzed *R*-band monitoring data spanning ten years of 31 blazars and found no strong evidence of periodicity in their sample. The γ-ray light curves of a sample of 10 blazars spanning ∼10 yr were analyzed, but no significant periodic pattern was seen (Covino et al. 2019). Moreover, in the VLBA light curve of PG 1553+113 that revealed QPO signals at γ-ray and optical frequencies (e.g., Ackermann et al. 2015; Tavani et al. 2018; Agarwal et al. 2021), there is no clear periodic pattern can be recognized (Lico et al. 2020). Even though the mechanism of the QPO is still up for discussion, studying the periodic pattern provides a good opportunity to learn more about the origin and nature of these sources.

Balzar PKS 0607–157 ($\alpha_{2000} = 06^{\rm h}09^{\rm m}40\overset{\rm s}{.}95$, $\delta_{2000} = -15°42'40\overset{''}{.}67$; QSO 0609–1542) is a nearby and highly variable source located at $z = 0.324$ (Jones et al. 2009). It was identified as a flat spectrum radio quasar (FSRQ), one subclass of blazars, as the presence of strong and broad emission lines produced by gas in the broad-line region (BLR). The central black hole mass was estimated to be $\sim 10^{7.32} M_\odot$ (Liu et al. 2006) and the total luminosity in BLR was estimated to have $L_{\rm BLR} = 10^{43.56}$ erg s^{-1} (Chai et al. 2012). PKS 0607–157 is known to have high and variable optical polarization, and has been classified as a radio intra-day variability (IDV) source with significant flux variability and variable polarization on both monthly and daily timescales (Kedziora-Chudczer et al. 2001). It was constrained to have low Doppler factor and was not detected at TeV energies (Finke 2019). The early works concerning this source mainly focused on the physical conditions and structure of the jet on parsec scale on the basis of the radio monitoring (e.g., Homan et al. 2001; Homan & Wardle 2003; Liu et al. 2006; Lister et al. 2011; Chai et al. 2012; Algaba et al. 2017; Finke 2019; Plavin et al. 2019). Although its characteristic timescales have not yet received much attention, it was found that PKS 0607–157 showed astrophysically meaningful periodicities of 10.9 ± 0.6 yr at 4.8 GHz, and 10.4 ± 0.7 and 6.5 ± 0.5 yr at 8.0 GHz radio frequency (Fan et al. 2007).

In this work, we made use of the radio observations from University of Michigan Radio Astronomical Observatory[1](UMRAO) at different frequencies to search for possible QPO of the blazar PKS 0607–157 on long-term timescale. We describe the observations and data reduction in Section 2, and present the resulting temporal analysis for periodicity by different methods in Section 3. In Section 4, we discuss possible scenarios for the detected QPOs and draw the conclusions.

2. Observations and Data Reduction

The source PKS 0607–157 was detected with the UMRAO 26 m paraboloid telescope located in Dexter, Michigan, USA, from 1983 to early 2010 s. Transistor-based radiometers are installed in the UMRAO telescope and operated at center frequencies of 4.8, 8.0, and 14.5 GHz with bandwidths of 0.68, 0.79, and 1.68 GHz, respectively. The UMRAO program used rotating, dual-horn polarimeter feed devices to measure the overall flux density and linear polarization of nearly two hundred AGNs. The continuing operation of UMRAO continually provided radio monitoring of PKS 0607–157, which makes it possible to search for QPO on long-term timescales. More details about the UMRAO program and data reduction can be found in Aller et al. (1985, 1999).

The obtained observations of PKS 0607–157 at 4.8, 8, and 14.5 GHz have been weekly averaged to smooth the short-term variabilities and form the light curves as shown in Figure 1. A visual examination on Figure 1 reveals that the light curves at various radio frequencies exhibit generally similar characteristics, and that a series of outbursts lasted for several months even years make it desirable to search for probable quasi-periodic flux modulations. Table 1 expresses the variability characteristics of radio light curves of PKS 0607–157, including number of the data, time span, flux range, average flux, and amplitudes. The amplitudes are quantified by variability amplitude (VA; Heidt & Wagner 1996) indicating peak-to-peak oscillation and the fractional variability amplitude $F_{\rm var}$ (Edelson et al. 2002) denoting average variability during the entire period. The amplitude VA is given by

$$VA = \sqrt{(A_{\max} - A_{\min})^2 - 2\sigma^2}, \tag{1}$$

where $A_{\max}$ and $A_{\min}$ are the maximum and minimum differential instrumental flux densities, respectively, while σ represents the mean errors in the light curves. $F_{\rm var}$ represents a measure of normalized excess variance and can be expressed as

$$F_{\rm var} = \sqrt{\frac{S^2 - \langle\sigma_{\rm err}^2\rangle}{\langle f\rangle^2}}, \tag{2}$$

for which the uncertainty is estimated by

$$\sigma_{F_{\rm var}} = \frac{1}{F_{\rm var}}\sqrt{\frac{1}{2N}}\frac{S^2}{\langle f\rangle^2}, \tag{3}$$

where S^2 is the sample variance, $\langle\sigma_{\rm err}^2\rangle$ the mean square uncertainty, and $\langle f\rangle$ the mean value of the measurements. The resulting VA and $F_{\rm var}$ for the radio light curves are listed in the last two columns of Table 1. Nevertheless, the analysis shows that the radio flux densities display remarkable variability with $F_{\rm var} > 30\%$, which makes it feasible to detect potential periodicities over the underlying noise.

3. Results

3.1. Flux Distribution

Some of the most significant hints to the origin and nature of blazar variability may be revealed by the study of their flux distributions. A statistical investigation of the probability density function (PDF) of fluxes can assist in restricting the fundamental mechanisms responsible for the observed blazar variabilities (e.g., Kushwaha et al. 2017; Sinha et al. 2018; Tavecchio et al. 2020). In general, normal PDF fitting of the flux distributions is typically thought to be created by linear additive processes, while log-normal distributions in blazars can be attributed to non-linear multiplicative processes, such as instability at the disk and jet, processes connecting the disk and jet, variable radiation from upscattered photons, extrinsic geometrical and projection effects, or coupling of the aforementioned processes (e.g., Shah et al. 2018; Bhatta & Dhital 2020). We investigated the radio flux distribution of this source by creating histograms to determine PDFs of the observations. In Figure 2, the PDFs of the radio fluxes at 4.8, 8.0, and 14.5 GHz of PKS 0607–157 are presented in histograms with 25 bins, and are fitted by log-normal (red lines) and normal (blue lines) functions. With a strong tail extending toward higher flux levels, all radio flux distributions are asymmetric. In our analysis, the log-normal model for PDF is given by

$$\mathrm{PDF}_{\rm log-normal}(x) = \frac{1}{\sqrt{2\pi}x\sigma}\exp\left[-\frac{(\ln x - \mu)^2}{2\sigma^2}\right], \tag{4}$$

[1] https://dept.astro.lsa.umich.edu/data sets/umrao.php

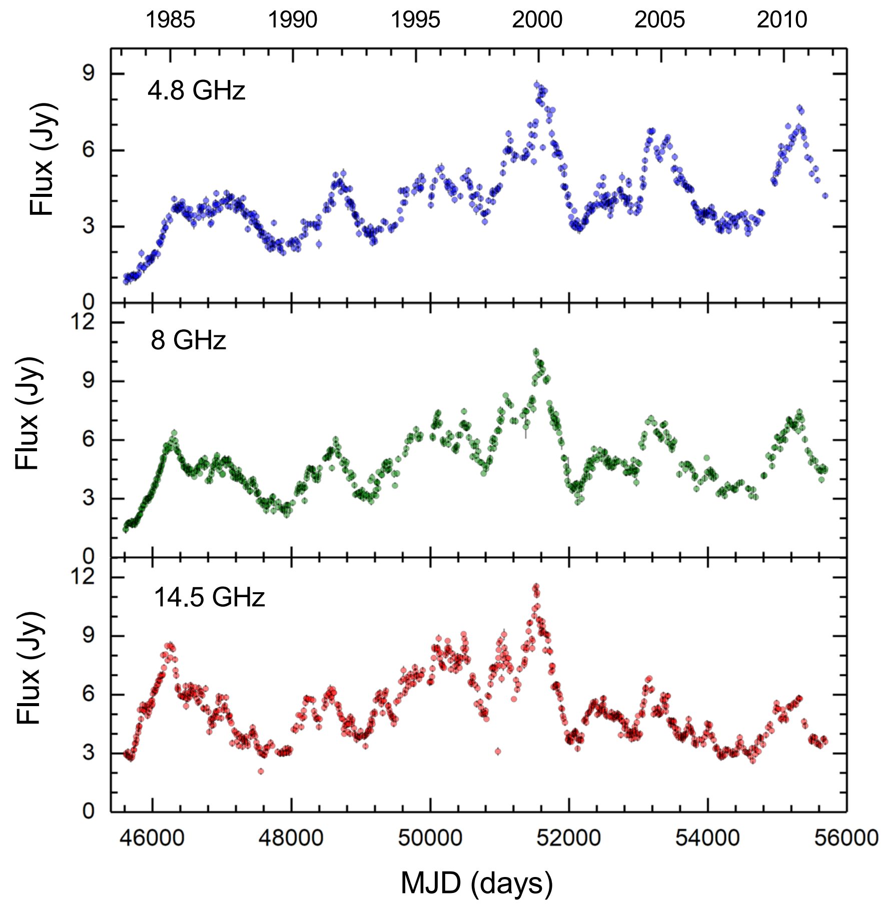

Figure 1. Weekly binned radio light curves of PKS 0607–157 obtained from the UMRAO. Panels (a), (b) and (c) represent fluxes at 4.8, 8, and 14.5 GHz spanning nearly 30 yr, respectively.

Table 1
Summary of the Radio Observations of PKS 0607–157 at 4.8, 8.0, and 14.5 GHz

Frequency (GHz)	Number	Time Span	Duration (yr)	Flux Range (Jy)	Average Flux (Jy)	VA (Jy)	F_{var} (%)
4.8	934	1983-10-8–2011-5-11	27.6	0.81–8.61	4.04	7.80	34.79 ± 1.02
8	939	1983-10-3–2011-5-2	27.6	1.14–10.55	4.86	9.14	32.58 ± 0.92
14.5	1084	1983-10-7–2011-5-10	27.6	2.08–11.54	5.35	9.46	31.57 ± 0.83

where σ and μ represent the scale parameter in units of flux and the mean flux location of the PDF in units of the natural log of flux, respectively. Similarly, the normal PDF has the form of

$$\mathrm{PDF}_{\mathrm{normal}}(x) = \frac{1}{\sqrt{2\pi}\,\sigma}\exp\left[-\frac{(\mathrm{x}-\mu)^2}{2\sigma^2}\right], \tag{5}$$

where σ and μ represent the standard deviation and the mean value of the PDF in units of flux, respectively. The best-fitting parameters for the log-normal and normal distribution as well as the reduced χ^2 obtained for these two models are given in Table 2. For all radio light curves, it can be found that the log-normal model is favored above the normal model according to the reduced χ^2. Then, the PDFs fitted with the log-normal model were used as inputs for light curve simulations in Sections 3.2 and 3.3.

3.2. Power Spectral Density Analysis

As one the most important characteristics of AGN variabilities, Power Spectral Density (PSD) has been widely used to investigate potential periodic modulations in time series contaminated by colored noise and/or white noise (e.g., Bhatta 2017; Li et al. 2017, and references therein). Random

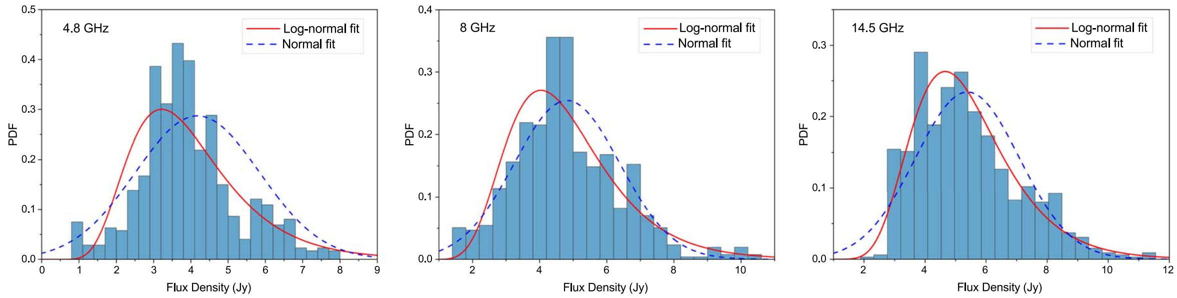

Figure 2. The normalized histogram of the radio fluxes at 4.8, 8.0, and 14.5 GHz with 25 bins. The red and blue lines represent the log-normal and normal PDF fitting to normalized histogram.

fluctuations induced by stochastic processes are often properly modeled as a power law $P(f) \propto f^{-\alpha}$ where $P(f)$ is the power at temporal frequency f with spectral index α. The underlying frequency-dependent noise is known as colored noise, particularly, red noise ($1 < \alpha \lesssim 2$) and white noise ($\alpha = 0$). For blazars, frequency-dependent noise dominates most light curves, especially in the low-frequency range, which must be dealt with seriously (e.g., Press 1978; Vaughan et al. 2016; Bhatta 2017; Covino et al. 2019; Li et al. 2021, 2023b). We applied Power Spectrum Response method (PSRESP; Uttley et al. 2002) to estimate the power spectral shape of the underlying power-law type noise for QPO analysis.

The PSRESP model has been frequently utilized to define PSDs of AGN periodograms using Monte Carlo simulations (e.g., Chatterjee et al. 2008; Max-Moerbeck et al. 2014; Bhatta et al. 2016; Ait Benkhali et al. 2020; Bhatta 2021; Goyal et al. 2022; Li et al. 2023a). In order to evaluate which model PSD has the highest likelihood of accurately representing the source PSD, the binned source periodogram is fitted with a variety of model PSDs with test parameters. In this work, a simple power law model with varying spectral index α was considered for the underlying power spectrum. The implementation of the PSRESP method is detailedly provided in (Uttley et al. 2002; Chatterjee et al. 2008; Bhatta et al. 2016). Some crucial specifics are as follows.

For a given time series $f(t_i)$ sampled at t_i with $j = 1, 2,..,N$ spanning a total duration of observations T, we calculated the normalized PSD at a temporal frequency ν using

$$P(\nu_k) = \frac{2T}{\mu^2 N^2} \left| \sum_{i=1}^{N} f(t_i) e^{-i2\pi\nu_k t_i} \right|^2, \tag{6}$$

with $\nu_k = k/T$, $k = 1,\ldots,N/2$, where the maximum frequency is the Nyquist frequency $\nu_{\rm Nyq} = N/2T$ and μ is the mean of the time series.

In order to obtain a χ^2-like statistic for the goodness-of-fit of the power-law model under consideration, we simulated 10,000 light curves for a particular test spectral index α. The χ^2-like statistic for each of the simulated light curves over the log-binned frequencies is given by

$$\chi^2_{\rm dist,i} = \sum_{\nu=\nu_{\min}}^{\nu_{\max}} \frac{[P_{\rm sim,i}(\nu) - \overline{P_{\rm sim}(\nu)}]^2}{\overline{\Delta P_{\rm sim}(\nu)}^2}, \tag{7}$$

where $P_{{\rm sim},i}(\nu)$, $\overline{P_{\rm sim}(\nu)}$ and $\overline{\Delta P_{\rm sim}(\nu)}$ are the PSD, mean PSD and standard deviation of all the simulated PSDs, respectively; i runs over the number of simulated light curves. Same as $\chi^2_{\rm dist}$, χ^2-like statistic for the observed light curve ($P_{\rm obs}(\nu)$) is defined as

$$\chi^2_{\rm obs} = \sum_{\nu=\nu_{\min}}^{\nu_{\max}} \frac{[P_{\rm obs}(\nu) - \overline{P_{\rm sim}(\nu)}]^2}{\overline{\Delta P_{\rm sim}(\nu)}^2}. \tag{8}$$

The artificial light curves are generated using the Emmanoulopoulos et al. (2013) implementation[2] coded by Connolly (2015). The Emmanoulopoulos algorithm is an enhancement to the method of Timmer & Koenig (1995) and is capable of reproducing light curves maintaining both the PDF and the power spectral of a light curve or a given model. The probability defined as the ratio of the number of $\chi^2_{\rm dist}$s greater than $\chi^2_{\rm obs}$ to the total number of $\chi^2_{\rm dist}$s distribution represents the goodness-of-fit.

We calculated the probabilities to determine the best fitting PSD model with a range of test spectral indices 1.0–3.0 in steps of 0.1 for the 4.8, 8.0, and 14.5 GHz light curves. The obtained results according to the PSRESP method are presented in Figure 3. In each panel, the red circles represent the best-fitting PSD model derived from the mean periodogram of 10,000 simulated light curves using the best-fitting model index, blue squares show the logarithmically binned source periodogram, gray line represents the source periodogram, respectively. The errors on the best-fitting PSD models are the standard deviations of the simulated periodograms from the averages. The inset in each panel shows probability distribution over the test spectral indices, from which the best-fitting model index can be derived. The best-fitting spectral indices and the corresponding highest probabilities (statistics for goodness-of-fit of PSD models) using the PSRESP method are represented in the last two columns of Table 2. The spectral index and its uncertainty were derived from the peak position and half-width

[2] https://github.com/samconnolly/DELightcurveSimulation

Table 2
The Best-fitting Parameters of the Radio Flux Distributions Fitted with Log-normal and Normal Models and the Corresponding Reduced χ^2 at Different Frequencies

Frequency	Log-normal			Normal			Spectral Index	Probability
(GHz)	μ[a]	σ	χ^2	μ[a]	σ	χ^2	α	(%)
4.8	1.32 ± 0.03	0.38 ± 0.02	54.00	3.98 ± 0.12	1.39 ± 0.08	61.41	1.88 ± 0.20	54.3
8	1.51 ± 0.03	0.34 ± 0.02	99.74	4.81 ± 0.12	1.87 ± 0.08	104.56	2.15 ± 0.35	50.8
14.5	1.64 ± 0.02	0.31 ± 0.02	85.38	5.38 ± 0.12	1.70 ± 0.08	147.92	1.76 ± 0.15	56.4

Note. The last two columns represent the best-fitting spectral indices and the corresponding highest probabilities of the probability distributions over the test spectral indices (see insets of Figure 3), according to the PSRESP method. The best-fitting spectral indices and the PDF parameters were used to simulate light curves for QPO significance estimation.
[a] in units of the natural log of flux.

at half maximum (HWHM) of the Gaussian fit for the probability distributions.

3.3. Periodicity Search

Combination of two conventional techniques, Weighted Wavelet Z-transform (WWZ; Foster 1996) and the Lomb-Scargle periodogram (LSP; Lomb 1976; Scargle 1982), was conducted to study the quasi-periodic behavior in the radio light curves of PKS 0607–157.

The LSP is a powerful tool widely used to detecting and characterizing periodicity in unevenly sampled light curves. LSP has been generalized for more practical use by Press & Rybicki (1989). The standard normalized LSP is equivalent to fitting sine waves of the form $y(t) = A\cos(\omega t) + B\sin(\omega t)$, and is defined for an uneven, simple time series (t_i, y_i) as

$$P(\omega) = \frac{\left[\sum_i y_i \cos(\omega(t_i - \tau))\right]^2}{2\sum_i \cos^2(\omega(t_i - \tau))} + \frac{\left[\sum_i y_i \sin(\omega(t_i - \tau))\right]^2}{2\sum_i \sin^2(\omega(t_i - \tau))}, \tag{9}$$

where τ is given by

$$\tan(\tau) = \frac{1}{2\omega}\frac{\sum_i \sin(2\omega t_i)}{\sum_i \cos(2\omega t_i)}. \tag{10}$$

More details are outlined in VanderPlas (2018) and references therein.

Unlike the classical LSP method, the WWZ algorithm analyze non-uniform astronomical data by capturing frequency and time information simultaneously in a contour plot, from which periodic modulations and their evolution with time can be determined. The WWZ method projects the time series onto three trial functions: $\phi_1(t) = 1(t)$, $\phi_2(t) = \cos[\omega(t - \tau)]$ and $\phi_3(t) = \sin[\omega(t - \tau)]$, with the statistical weights given by $\omega_\alpha = \exp(-c\omega^2(t_\alpha - \tau)^2)$ $(\alpha = 1, 2, 3)$ on the projection, where c is determined by the rate of Morlet wavelet decays. The Morlet kernel has the form

$$f[\omega(t - \tau)] = e^{i\omega(t-\tau) - c\omega^2(t-\tau)^2}. \tag{11}$$

Then the WWZ power is defined as

$$\mathrm{WWZ} = \frac{(N_{\mathrm{eff}} - 3)V_y}{2(V_x - V_y)}, \tag{12}$$

where N_{eff} denotes the effective number of data points, and V_x and V_y are the weighted variations and the model function, respectively. Many earlier publications, such as Foster (1996), An et al. (2013), Bhatta et al. (2016), Sarkar et al. (2020), Roy et al. (2022), have further information concerning the WWZ approach.

We applied the WWZ approach to the radio light curves with a limited frequency range of 0.00025–0.01 day^{-1}, a period step of 10 days and a decay constant $c = 0.001$. In addition, by averaging the WWZ power spectrum across certain frequencies/periods, the time-averaged WWZ power spectrum can be calculated without considering their evolution with time. In time-averaged WWZ power spectrum, distinct peaks with high WWZ power can be considered as candidate QPOs.

We first examine the existence of the periodic modulations for the multi-band radio light curves and represent the resulting WWZ and LSP analyses in Figure 4. Color contour of the WWZ power spectrum calculated for the 4.8-GHz light curve is shown in left part of panel (a), which reveals large WWZ power centered around the periods of about 1700 days and 2100 days. Particularly, it can be found that a remarkable periodicity of ∼1700 days modulated in the whole observation. In right part of panel (a), the time-averaged WWZ power spectrum (red solid line) reveal distinct and significant peaks centered at the periods of about 1700 days and 2100 days, which is generally consistent with the LSP power spectrum (blue dotted line).

Periodicity analysis for 8.0 and 14.5 GHz light curves are shown in panel (b) and panel (c) of Figure 4, respectively. In panel (b) analyzed for 8.0-GHz light curve, considerable WWZ power centered around 1700 days persisting throughout the whole observation, which has been verified by the time-averaged WWZ power spectrum and the LSP power spectrum represented in the right part. Similarly, panel (c) demonstrates the WWZ and LSP analyses for the 14.5 GHz light curve, in which a prominent periodicity of about 1700 days persisting first and middle half of the observation can be derived from the

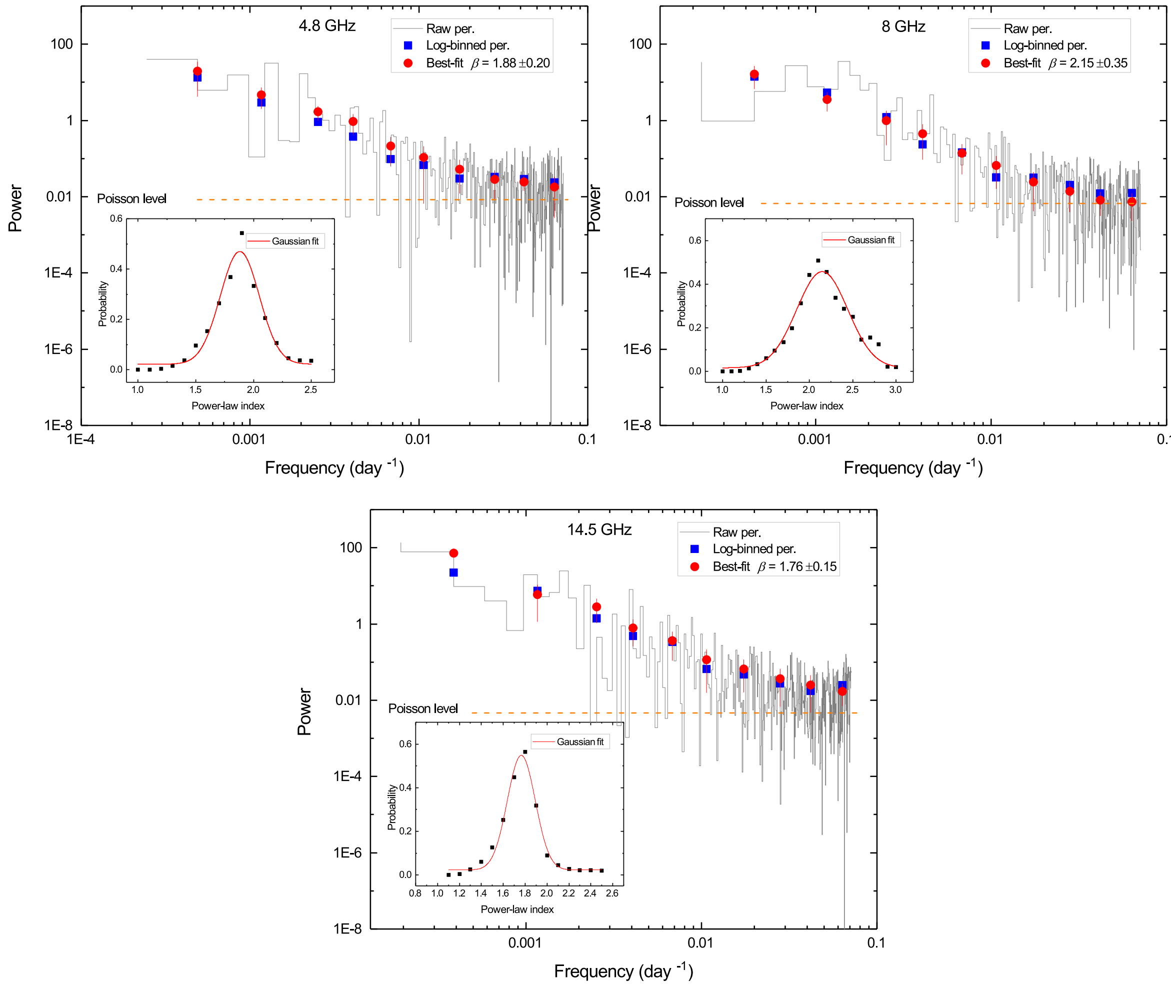

Figure 3. Result of application of the PSRESP method to the radio fluxes at 4.8, 8.0, and 14.5 GHz of PKS 0607–157. The gray lines show the source periodogram, while the blue squares and red circles express the logarithmically binned source periodogram and the fitted power spectrum using the best-fitting index, respectively. The errors on indices correspond to the standard deviations of the best-fitting simulated PSDs. Following PSRESP method, the inset in each panel represents the probability distribution with spectral indices ranging from 1.0 to 3.0 in steps of 0.1. The red solid lines are the Gaussian functions fitted to the data.

color contour. In the right part of panel (c), these periodic modulations have also been revealed by the LSP power spectrum and time-averaged WWZ power spectrum.

In order to assess the significance of the potential QPOs detected above, we applied a large number of Monte Carlo simulations to establish the colored noise background by randomizing the amplitude and the phase of the Fourier components and considering the PDFs of the light curves, following the widely used prescriptions by Emmanoulopoulos et al. (2013). For each wave band, we simulated 10^6 light curves using the log-normal PDF fitting parameters and the best-fit PSD model (see Table 2). The simulated light curves mimic several properties of the original light curves, such as PDF, PSD, mean, standard deviation, sampling pattern, and observation duration. A series of LSP and time-averaged WWZ power spectrum were produced by using the same procedure on each simulated light curve. The percentiles of the power at each frequency/period were used to establish the LSP and WWZ confidence levels from the simulated LSP and WWZ periodograms, respectively. In this work, a significant QPO is one whose LSP and time-averaged WWZ power peaks simultaneously reach the corresponding 3σ LSP and WWZ confidence level.

In each panel of Figure 4, the 3σ WWZ and LSP confidence curves are plotted as magenta dashed line and green dashed–dotted line over the corresponding periodograms, respectively. As shown in panel (a), a QPO with high power amplitude at 1670 ± 100 days mentioned above are detected above the 3σ LSP and WWZ confidence level simultaneously, while QPOs of 2140 ± 150 days stayed below the confidence criterion. For the analysis of 8.0 GHz light curve (panel (b)), potential QPO centered at 1680 ± 110 days can be detected above a 3σ confidence curve in both WWZ and LSP analyses. As for the significance estimation for the 14.5 GHz light curve, we have

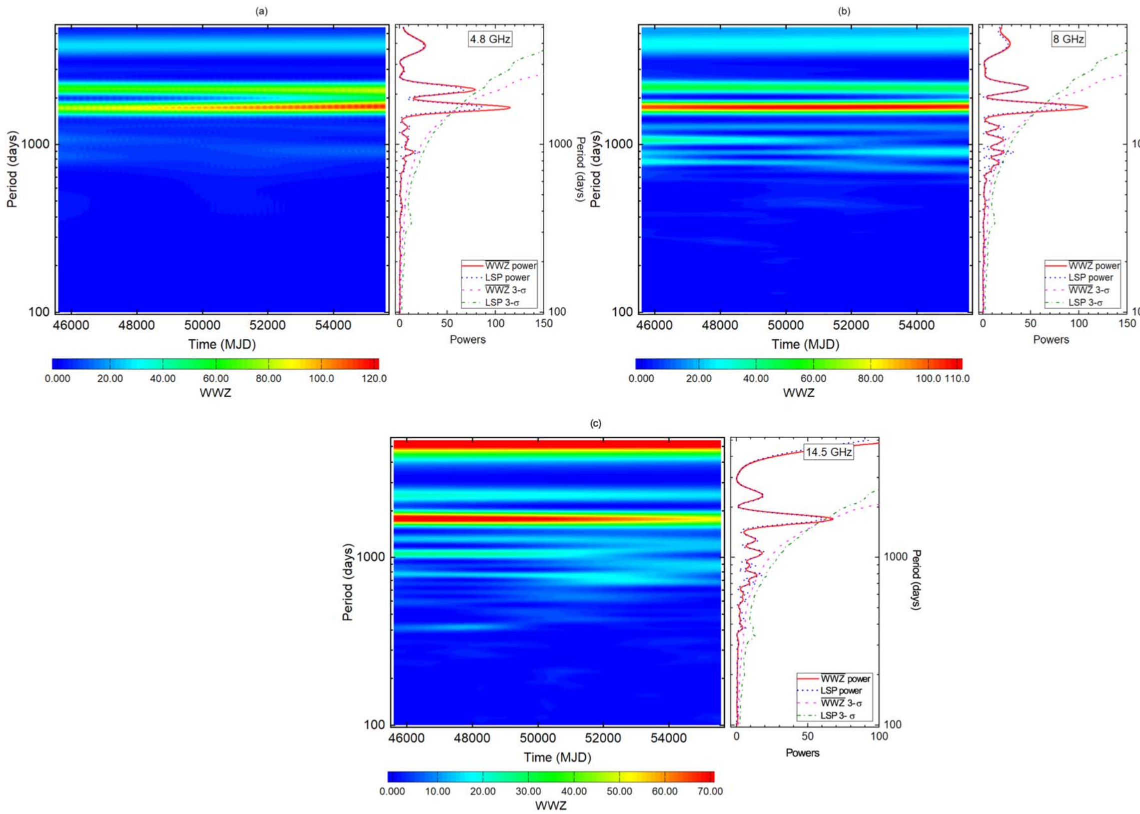

Figure 4. Panel (a), (b) and (c) represent the periodicity analysis and significance estimation for the weekly binned 4.8 , 8.0 and 14.5 GHz light curves, respectively. In each panel, the color contour shows the WWZ power spectrum calculated for the radio light curve in time-period plane; the periodogram represents the time-averaged WWZ power (red solid line) and the LSP power (blue dotted line) as well as the corresponding 3σ WWZ and LSP confidence contours (magenta dashed line and green dashed–dotted line) from the Monte Carlo simulations.

found the evidence that periodicity of 1700 ± 130 days are slightly above the 3σ level in both WWZ and LSP estimations, as shown in panel (c). The periodicities and their uncertainties were estimated by the peak positions and HWHMs of the Gaussian fits for the corresponding WWZ power peaks.

4. Discussion and Conclusions

We have carried out a periodicity analysis of long-term UMRAO radio observations of the blazar PKS 0607–157. The observations at 4.8, 8.0 and 14.5 GHz covering 1983–2011 present a generally consistent feature, exhibiting several drastic flaring events with duration of months, even years. The flux densities variability amplitudes $F_{\rm var}$s at different radio frequencies were measured to be >30%. It was found that the log-normal model is preferred over the normal model for all radio light curves. According to the PSRESP method, the PSDs for the 4.8, 8.0, and 14.5 GHz light curves can be well fitted with a simple power-law with spectral indices of 1.88 ± 0.20, 2.15 ± 0.35 and 1.76 ± 0.15, respectively.

We employed the WWZ and LSP methods to detect possible QPO in the radio light curves. With the best-fitting PDF and PSD model parameters, we totally generated 3×10^6 light curves using Monte-Carlo simulation to account for the underlying colored-noise spectrum background. In the 4.8, 8, and 14.5 GHz light curves, our results show QPO signals of 1670 ± 100 days, 1680 ± 110 days and 1700 ± 130 days at a significance of 3σ, respectively. Given the closeness of the UMRAO frequencies, it is more likely that these QPOs have similar physical origin. Then, we conclude that a possible QPO of about ∼4.6 yr (averaged for the all bands) exhibited in the UMRAO radio light curves of PKS 0607–157. The QPO signal observed in this study appears to be potentially associated with a harmonic of the 10.9 yr and 10.4 yr QPO periods reported by Fan et al. (2007), within the error range. However, the possibility of their identification of the QPO as a harmonic needs to be carefully considered, as the ∼10 yr QPO period they reported may have been overestimated due to the analysis spanning approximately 25 yr. Furthermore, our Figure 4 does not support the existence of a ∼10 yr QPO when considering the confidence criterion. This discrepancy may arise from the complex variability behavior in blazars and the different time ranges used in the two QPO search analyses.

Over the past few decades, quasi-periodic signals have been detected across the entire electromagnetic spectrum and on all accessible timescales. Despite the fact that blazar emission processes are not well known, several physical models are proposed to explain the mechanisms of quasi-periodic emission in blazars, such as the origin and inner structure of the jets (e.g., Mohan & Mangalam 2015; Sobacchi et al. 2017; Otero-Santos et al. 2020; Sarkar et al. 2021), dynamical, thermal, and viscous processes occurring in accretion disks (e.g., Gupta et al. 2009; Wang et al. 2014; Kaur et al. 2017; Liska et al. 2018), constraints on diskjet connection (e.g., An et al. 2013; King et al. 2013; Sandrinelli et al. 2016), supermassive binary black hole (SMBBH) systems (e.g., Ackermann et al. 2015; Sobacchi et al. 2017; Caproni et al. 2017; Li et al. 2018; Ren et al. 2021). The accretion disk instabilities scenario are often ascribed to QPOs with timescales of one year and less (e.g., Rani et al. 2010; Gupta et al. 2012; Bhatta et al. 2016; Kushwaha et al. 2020). Particularly, long-term periodic modulations may be produced in a binary black hole system by the orbital motion causing periodic accretion disturbances, or by jet-precessional and nutational movements (e.g., Rieger 2004, 2007; Mohan & Mangalam 2015; Liska et al. 2018). In this work, we explain the detected radio QPO of ∼4.6 yr as the results of an SMBBH system, Lense-Thirring precession of the disk, and helical motion of plasma blobs within the jet.

The first periodic driving scenario we discussed here is the SMBBH model. The long-term periodic flux modulations can be due to the orbital motion inducing periodic accretion perturbations, or jet-precessional and nutational motions (e.g., Ackermann et al. 2015; Caproni et al. 2017; Bhatta & Dhital 2020; Bhatta 2021; Sarkar et al. 2021; Li et al. 2023b). If the detected QPOs result from the Keplerian orbital motion of the secondary black hole around the primary one in a SMBBH system, it becomes possible to estimate the orbital parameters. The intrinsic orbital timescale in the rest frame of the source at a redshift of z is given by $P = P_{\rm obs}/(1+z)$, where $P_{\rm obs}$ represents the observed period. According to Kepler's law, the semimajor axis of the binary system, denoted as a, can be estimated using the equation $P^2 = 4\pi^2 a^3/{\rm G}(m+M)$, where M and m represent the masses of the primary and secondary black holes, respectively, and G is the gravitational constant. Applying this relationship to the observed period, it suggests a tightly bound orbit with a binary separation of approximately 1856 gravitational radii (r_g), or equivalently, ∼0.0037 pc. For this estimation, we assume a binary mass ratio of $m/M = 0.01$, and the mass of the central black hole is chosen to be $M = 10^{7.32} M_\odot$ (Liu et al. 2006).

In blazars, a number of effects, such as Lense-Thirring or spinstellar disk interaction can lead to a jet precessions, thereby, resulting in the quasi-periodic modulation (see Sobacchi et al. 2017; Liska et al. 2018, and references therein). In the strong gravitational field of a fast-spinning central SMBH, the nearby inertial frames are distorted by the central SMBH due to the frame-dragging effect. The inner region of the accretion disk may be warped due to the frame dragging effect, which might result in the nodal precession of the tilted plane of the disk, known as the Lense-Thirring precession (e.g., Stella & Vietri 1998; Fragile & Meier 2009; Motta et al. 2011). In this scenario, the wriggling of the jet may provide quasi-periodic contributions to the observed variabilities. For QPOs seen in stellar-mass black hole systems and quasi-periodic signal found in blazars, the Lense-Thirring scenario has received much attention (e.g., King et al. 2013; Sandrinelli et al. 2016; Sobacchi et al. 2017; Liska et al. 2018; Bhatta & Dhital 2020). The Lense Thirring precession period scales as

$$P_{\rm LT} = \frac{8\pi GM}{c^3 a}\left(\frac{r}{r_g}\right)^3, \tag{13}$$

where a and M denote the spin parameter and mass of SMBH, and r is the radial distance to the black hole, respectively. In the case of geometrically thick accretion flows, the inner disk precesses as a solid body and the size of the inner precessing region can be estimated from the observed period. A detected quasi-periodic timescale of ∼4.6 yr places the emission region around 34 r_g (Schwarzschild radius) for a maximally parameter of $a = 0.9$, central black hole with a mass of $M = 10^{7.32} M_\odot$ (Liu et al. 2006). Then, the jet precession that causes the periodic oscillations may have occurred due to the warped accretion disks. Here, the observed quasi-periodic timescale $P_{\rm obs}$ is corrected to the intrinsic period $P = P_{\rm obs}/(1+z)$ for the cosmological redshift.

As a high-luminosity blazar, flux variations of PKS 0607–157 could be due to the changes of the viewing angle, emission blobs or perturbations propagating along a precessing, bent or helical jet. A second scenario we discussed here is that the observed QPO is related to plasma blobs (or enhanced emission) moving helically in the jet, which has been utilized to explain the possible QPOs in blazars (e.g., Mohan & Mangalam 2015; Zhou et al. 2018; Sarkar et al. 2020, 2021; Yang et al. 2021; Li et al. 2021; Gong et al. 2023). Due to the helical motion of the plasma blob, the viewing angle $\theta_{\rm obs}(t)$ of an emitting blob's helical motion depends on the observed period $P_{\rm obs}$, pitch angle ϕ between the emitting blob's motion and the jet's axis, and the inclination angle ψ of the jet to the observers, which is given by (e.g., Sobacchi et al. 2017; Zhou et al. 2018)

$$\cos\theta_{\rm obs}({\rm t}) = \sin\phi\,\sin\psi\,\cos(2\pi{\rm t}/{\rm P_{obs}}) + \cos\phi\,\cos\psi. \tag{14}$$

The Doppler factor varies with the viewing angle as $\delta(t) = [\Gamma(1-\beta\cos\theta_{\rm obs}(t))]^{-1}$, where $\Gamma = (1-\beta^2)^{-1/2}$ is the bulk Lorentz factor of the blob motion with normalized velocity $\beta = v_{\rm jet}/c$. Then the period in the rest frame of the blob can be expressed as,

$$P = \frac{P_{\rm obs}}{1-\beta\cos\psi\cos\phi}. \tag{15}$$

Using $\phi = 17^\circ\!.5$, $\psi = 5^\circ$ and $\Gamma = 3.9$ (Lister et al. 2011; Chai et al. 2012), the periodicity in the blob rest-frame is estimated to be 56 yr for $P_{\mathrm{obs}} = 4.6$ yr. The blob traverses about a distance $D = c\beta P\cos\phi \approx 16$ pc propagating down the jet during one cycle. In this scenario, the injected blob increases the jet brightness and travels helically inside the jet until the blob dissipates, which provides a reasonable explanation for the detected QPO. In this work, we briefly discussed three plausible interpretations. However, the current QPO models are still under debate, the observed QPOs in blazars could be ascribed to a combination of different physical mechanisms.

Acknowledgments

This work was funded by the National Natural Science Foundation of China (NSFC) under No.11903028. X.-P. LiX.-P.L. acknowledges the support from the "Yunnan Revitalization Talent Support Program" of Yunnan province, China. We are very grateful to Dr. Margo Aller for providing the UMRAO data. This research has made use of data from the University of Michigan Radio Astronomy Observatory, which is supported by the University of Michigan and by a series of grants from the National Science Foundation, most recently AST-0607523, and NASA Fermi grants NNX09AU16G, NNX10AP16G, and NNX11AO13G. Light curve simulation and significance estimation were performed on the key laboratory of high density computing, Zhaotong University. The authors sincerely thank the anonymous reviewer for constructive comments and suggestions that greatly improved this manuscript.

References

Ackermann, M., Ajello, M., Albert, A., et al. 2015, ApJL, 813, L41
Agarwal, A., Mihov, B., Andruchow, I., et al. 2021, A&A, 645, A137
Ait Benkhali, F., Hofmann, W., Rieger, F. M., & Chakraborty, N. 2020, A&A, 634, A120
Algaba, J. C., Nakamura, M., Asada, K., & Lee, S. S. 2017, ApJ, 834, 65
Aller, H. D., Aller, M. F., Latimer, G. E., & Hodge, P. E. 1985, ApJS, 59, 513
Aller, M. F., Aller, H. D., Hughes, P. A., & Latimer, G. E. 1999, ApJ, 512, 601
An, T., Baan, W. A., Wang, J.-Y., Wang, Y., & Hong, X.-Y. 2013, MNRAS, 434, 3487
Bhatta, G. 2017, ApJ, 847, 7
Bhatta, G. 2021, ApJ, 923, 7
Bhatta, G., & Dhital, N. 2020, ApJ, 891, 120
Bhatta, G., Zola, S., Stawarz, Ł., et al. 2016, ApJ, 832, 47
Caproni, A., Abraham, Z., Motter, J. C., & Monteiro, H. 2017, ApJL, 851, L39
Chai, B., Cao, X., & Gu, M. 2012, ApJ, 759, 114
Chatterjee, R., Jorstad, S. G., Marscher, A. P., et al. 2008, ApJ, 689, 79
Connolly, S. D. 2015, arXiv:1503.06676
Covino, S., Sandrinelli, A., & Treves, A. 2019, MNRAS, 482, 1270
Edelson, R., Turner, T. J., Pounds, K., et al. 2002, ApJ, 568, 610
Emmanoulopoulos, D., McHardy, I. M., & Papadakis, I. E. 2013, MNRAS, 433, 907
Fan, J. H., Liu, Y., Yuan, Y. H., et al. 2007, A&A, 462, 547
Finke, J. D. 2019, ApJ, 870, 28
Foster, G. 1996, AJ, 112, 1709
Fragile, P. C., & Meier, D. L. 2009, ApJ, 693, 771
Gong, Y., Tian, S., Zhou, L., Yi, T., & Fang, J. 2023, ApJ, 949, 39
Goyal, A., Soida, M., Stawarz, Ł., et al. 2022, ApJ, 927, 214
Goyal, A., Stawarz, Ł., Zola, S., et al. 2018, ApJ, 863, 175
Gupta, A. C., Krichbaum, T. P., Wiita, P. J., et al. 2012, MNRAS, 425, 1357
Gupta, A. C., Srivastava, A. K., & Wiita, P. J. 2009, ApJ, 690, 216
Heidt, J., & Wagner, S. J. 1996, A&A, 305, 42
Homan, D. C., Attridge, J. M., & Wardle, J. F. C. 2001, ApJ, 556, 113
Homan, D. C., & Wardle, J. F. C. 2003, A&SS, 288, 29
Jones, D. H., Read, M. A., Saunders, W., et al. 2009, MNRAS, 399, 683
Kaur, N., Sameer, B. K. S., & Ganesh, S. 2017, MNRAS, 469, 2305
Kedziora-Chudczer, L. L., Jauncey, D. L., Wieringa, M. H., Tzioumis, A. K., & Reynolds, J. E. 2001, MNRAS, 325, 1411
King, O. G., Hovatta, T., Max-Moerbeck, W., et al. 2013, MNRAS, 436, L114
Kushwaha, P., Sarkar, A., Gupta, A. C., Tripathi, A., & Wiita, P. J. 2020, MNRAS, 499, 653
Kushwaha, P., Sinha, A., Misra, R., Singh, K. P., & de Gouveia Dal Pino, E. M. 2017, ApJ, 849, 138
Li, X.-P., Cai, Y., Yang, H.-T., et al. 2021, MNRAS, 506, 1540
Li, X.-P., Cai, Y., Yang, H.-Y., et al. 2023a, MNRAS, 519, 4893
Li, X.-P., Luo, Y.-H., Yang, H.-Y., et al. 2017, ApJ, 847, 8
Li, X.-P., Luo, Y.-H., Yang, H.-Y., et al. 2018, A&SS, 363, 169
Li, X.-P., Yang, H.-Y., Cai, Y., et al. 2023b, ApJ, 943, 157
Lico, R., Liu, J., Giroletti, M., et al. 2020, A&A, 634, A87
Liska, M., Hesp, C., Tchekhovskoy, A., et al. 2018, MNRAS, 474, L81
Lister, M. L., Aller, M., Aller, H., et al. 2011, ApJ, 742, 27
Liu, Y., Jiang, D. R., & Gu, M. F. 2006, ApJ, 637, 669
Lomb, N. R. 1976, A&SS, 39, 447
Max-Moerbeck, W., Richards, J. L., Hovatta, T., et al. 2014, MNRAS, 445, 437
Mohan, P., & Mangalam, A. 2015, ApJ, 805, 91
Motta, S., Muñoz-Darias, T., Casella, P., Belloni, T., & Homan, J. 2011, MNRAS, 418, 2292
Nilsson, K., Lindfors, E., Takalo, L. O., et al. 2018, A&A, 620, A185
Otero-Santos, J., Acosta-Pulido, J. A., Becerra González, J., et al. 2020, MNRAS, 492, 5524
Peñil, P., Domínguez, A., Buson, S., et al. 2020, ApJ, 896, 134
Plavin, A. V., Kovalev, Y. Y., Pushkarev, A. B., & Lobanov, A. P. 2019, MNRAS, 485, 1822
Press, W. H. 1978, ComAp, 7, 103
Press, W. H., & Rybicki, G. B. 1989, ApJ, 338, 277
Rani, B., Gupta, A. C., Joshi, U. C., Ganesh, S., & Wiita, P. J. 2010, ApJL, 719, L153
Ren, G.-W., Ding, N., Zhang, X., et al. 2021, MNRAS, 506, 3791
Rieger, F. M. 2004, ApJL, 615, L5
Rieger, F. M. 2007, A&SS, 309, 271
Roy, A., Sarkar, A., Chatterjee, A., et al. 2022, MNRAS, 510, 3641
Sandrinelli, A., Covino, S., Dotti, M., & Treves, A. 2016, AJ, 151, 54
Sandrinelli, A., Covino, S., Treves, A., et al. 2018, A&A, 615, A118
Sarkar, A., Gupta, A. C., Chitnis, V. R., & Wiita, P. J. 2021, MNRAS, 501, 50
Sarkar, A., Kushwaha, P., Gupta, A. C., Chitnis, V. R., & Wiita, P. J. 2020, A&A, 642, A129
Scargle, J. D. 1982, ApJ, 263, 835
Shah, Z., Mankuzhiyil, N., Sinha, A., et al. 2018, RAA, 18, 141
Sinha, A., Khatoon, R., Misra, R., et al. 2018, MNRAS, 480, L116
Sobacchi, E., Sormani, M. C., & Stamerra, A. 2017, MNRAS, 465, 161
Sobolewska, M. A., Siemiginowska, A., Kelly, B. C., & Nalewajko, K. 2014, ApJ, 786, 143
Stella, L., & Vietri, M. 1998, ApJL, 492, L59
Tavani, M., Cavaliere, A., Munar-Adrover, P., & Argan, A. 2018, ApJ, 854, 11
Tavecchio, F., Bonnoli, G., & Galanti, G. 2020, MNRAS, 497, 1294
Timmer, J., & Koenig, M. 1995, A&A, 300, 707
Urry, C. M., & Padovani, P. 1995, PASP, 107, 803
Uttley, P., McHardy, I. M., & Papadakis, I. E. 2002, MNRAS, 332, 231
VanderPlas, J. T. 2018, ApJS, 236, 16
Vaughan, S., Uttley, P., Markowitz, A. G., et al. 2016, MNRAS, 461, 3145
Wang, J.-Y., An, T., Baan, W. A., & Lu, X.-L. 2014, MNRAS, 443, 58
Yang, J., Cao, G., Zhou, B., & Qin, L. 2021, PASP, 133, 024101
Zhang, P.-f., Yan, D.-h., Liao, N.-h., & Wang, J.-c. 2017, ApJ, 835, 260
Zhou, J., Wang, Z., Chen, L., et al. 2018, NatCo, 9, 4599